

Uniform Longitudinal Zinc Growth beyond Interface Guided by Anionic Covalent Organic Framework for Dendrite-Free Aqueous Zinc Batteries

Xiaoqi Wang,^[a, c] Pengpeng Shao,^[a] Shengchi Bai,^[c] Rui Yang,^[c] Xu Jin,^[c] Chunyi Zhi,*^[b] and Bo Wang*^[a]

Aqueous zinc (Zn) batteries hold considerable promise to address safety problems that frequently occur in electric vehicle cells or energy storage applications. However, Zn metal anode suffers seriously from dendrite, corrosion, and interface water decomposition in aqueous electrolytes, especially under large areal capacity or long charging duration. This is mainly because of the uneven longitudinal Zn growth induced by the anisotropic Zn^{2+} diffusion, which is usually neglected in a laboratory study with low areal capacity. Herein, we report an artificial interface of the anodic covalent organic framework (COF, which can be rapidly synthesized and facilely assembled with Zn anode in a large area) to guide the uniform longitudinal Zn growth for dendrite-free Zn batteries. In-situ optical micro-

scope observes that compared with the bare Zn anode, COF interface can promote the formation of the smooth and dendrite-free surface through spatial-triggered uniform longitudinal Zn growth. Theoretical calculation uncovers that anodic COF with a negative charge at its N sites could attract Zn^{2+} to achieve uniform longitudinal Zn^{2+} diffusion. In addition, this COF interface with superior hydrophobicity could suppress water decomposition and Zn corrosion. Consequently, the COF-functionalized Zn anode realizes a high coulombic efficiency under severe Zn plating/stripping conditions (10 mAh cm^{-2}), contributing to a long Zn-I₂ full battery life of over 10000 cycles. This work highlights the high-areal-capacity Zn anode protection in external space beyond the interface.

Introduction

Clean electricity generated from renewable solar or wind energy plays a significant role in achieving the goal of carbon peaking and carbon neutralization. Due to the volatility and intermittency of renewable energy, however, large-scale energy storage technologies are urgently needed to solve electricity-related strategic issues such as large-scale access to renewable energy, coupled utilization of multi-energy, and deep electrification of terminal energy consumption.^[1–4] Up to now, lithium-ion batteries (LIBs) have dominated markets of mainstream energy storage products in different scenarios, including mobile phones, electric vehicles, and energy storage power stations. However, LIBs have frequently been undergoing safety accidents such as explosion and spontaneous combustion mainly due to the inflammable organic electrolytes, which have

aroused great concern about the safety of batteries.^[1] Aqueous Zn batteries (AZBs) that run in intrinsically safe water-dominated electrolytes, can fundamentally solve safety problems.^[1,5–7] In addition, this aqueous regime could avoid the strict manufacturing conditions and fundamentally improve the power characteristics of the battery system benefitting from the superior ionic conductivity that is 2 orders of magnitude higher than organic electrolytes.^[8–10] Moreover, Zn metal with a low redox potential (-0.76 V vs. standard hydrogen electrode, SHE) and a high capacity (820 mAh g^{-1}) can release high energy in aqueous electrolytes.^[11] The development of cathode materials such as ion intercalation type manganese oxides,^[12–14] Prussian blue analogues (PBA),^[15] vanadium oxides,^[16,17] and organics^[18,19] also promote the rapid advance of AZBs. Therefore, AZBs are spurring extensive interest in the battery community to meet the requirements of efficient and safe energy storage.

Despite the multiple merits mentioned above, AZBs still suffer seriously from the Zn anode challenges such as poor stability and electrochemical reversibility due to the Zn dendrite growth and corrosion.^[20,21] This was widely accepted by previous works as comprehensive results of the uneven Zn^{2+} gradient, electric field, and interface pH change.^[22–24] To address these issues, Zn anode design including artificial interface construction, three-dimensional substrate, and alloy anode could realize uniform nucleation and lower the localized current density.^[9,25–27] In addition, electrolyte modification through adding high-concentration salts or organic molecules could effectively tune the solvation structure of zinc ions and promote the formation of solid electrolyte interface (SEI).^[28–30]

[a] X. Wang, Dr. P. Shao, Prof. B. Wang
School of Chemistry and Chemical Engineering
Beijing Institute of Technology
Beijing 100081 (P. R. China)
E-mail: bowang@bit.edu.cn

[b] Prof. C. Zhi
Department of Materials Science and Engineering
City University of Hong Kong
83 Tat Chee Avenue, Kowloon, Hong Kong SAR (China)
E-mail: czhi@cityu.edu.hk

[c] X. Wang, Dr. S. Bai, R. Yang, Dr. X. Jin
Research Institute of Petroleum Exploration & Development (RIPED)
China National Petroleum Corporation
Beijing, 100083 (P. R. China)

 Supporting information for this article is available on the WWW under
<https://doi.org/10.1002/batt.202300099>

Separator functionalization with surface chemistry and pore structure could accelerate the desolvation of hydrated Zn^{2+} .^[31–33] These strategies improve the cycling stability and reversibility of Zn metal anode.

Nevertheless, it still remains as a challenge to achieve a practical Zn anode with large areal capacity or high depth of discharge (DOD) which is as pursued required by practical use.^[20] This is because current dendrite protection methods mainly concentrate on the Zn deposition behavior at the anode/electrolyte interface where a thin thickness ($<1\ \mu m$) of Zn deposit corresponds to a low capacity of $<0.585\ mAh\ cm^{-2}$. The further extra charging capacity depends on the longitudinal Zn growth in the external space beyond the interface, which is likely to promote the inundation of Zn dendrite once without any external protection. Longitudinal Zn growth in the external space beyond the interface is the key step for practical Zn anode with large areal capacity, which has never been studied before. Covalent organic frameworks (COFs), as an emerging class of polymeric materials, are recently reported to be promising in constructing protective layers for the Zn anode in AZBs, due to their advantages in designable structures to become Zn affinity, ability to effectively homogenize the distribution of Zn^{2+} flux and space electric field, and capability to remove the Zn solvated water in the bulk electrolyte.^[34–36] Therefore, using COFs to form an interlayer to guide the longitudinal Zn growth is speculated to be feasible.

In this work, we report the uniform longitudinal Zn growth in the external space beyond the interface by introducing anodic TAPB-PDA COF linked by 1,3,5-tris (4-aminophenyl) benzene (TAPB) and terephthalaldehyde (PDA). Rapid synthesis and facile integration with Zn foil of COF were reported. In situ optical microscope observation was conducted to real-time investigate the longitudinal Zn growth behavior by gradually increasing the capacity to a high value of $10\ mAh\ cm^{-2}$. Theoretical computation was employed to study the center of the negative charge in COF and calculate the binding strength between COF and zinc. We also examined the hydrophilicity of COF to test its influence on the Zn corrosion behavior and the possible suppression of alkaline zincate formation on Zn anode surface. Finally, the general dendrite protection of COF was confirmed by symmetric cell and Zn-I₂ full batteries with long life of more than 10000 cycles.

Results and Discussion

TAPB-PDA COF was rapidly (in about 10 min) synthesized based on the reaction of solvothermal condensation using aldehyde and aniline monomers at room temperature.^[37] It has 2D anionic crystalline networks with in-plane pores which can serve as the ion diffusion channels as schematically shown in Figure 1(a). This COF was rapidly synthesized in 10 min (Figure 1a), demonstrating a good capability for practical use from the perspective of production cycle. Scanning electron microscope (SEM) image shows the morphology of TAPB-PDA COF (Figures 1b, S1), the EDS mapping shows the uniform distribution of C, O, and N elements (Figure 1c). The crystallinity was

determined by powder X-ray diffraction (PXRD, Figure 1d) pattern, where sharp peaks match well with the calculated result.^[37] The specific surface area (SSA) was tested to be as high as $1267.7\ m^2\ g^{-1}$ and the pore structure mainly consists of micropores with pore sizes of $3.4\ nm$ as determined by non-local density functional theory (NLDFT) model (Figure 1e). X-ray photoelectron spectroscopy (XPS) was used to analyze the surface chemistry of the TAPB-PDA COF (Figure S2). The high-resolution C1s spectrum (Figure 1f) uncovers the typical C=N and C–C groups, directly confirming the covalent coupling between TAPB and PDA units for establishing TAPB-PDA COF. In addition, the high-resolution N1s spectrum (Figure 1g) confirms the existence of C=N and N–H groups, while N–H corresponds to some unreacted –NH₂ groups. The molecular chemistry of TAPB-PDA COF was studied by the Fourier-transform infrared (FTIR) spectrum, which shows apparent peaks at 970 , 1561 , and $1700\ cm^{-1}$, which correspond to the typical stretch of the TAPB-PDA COF (Figure 1h).^[37] The TAPB-PDA COF was then pasted onto the Zn anode using PVDF as binder and NMP as a dispersion agent. Notably, this assembly was developed into a scaleup preparation process (Figure 1i), which enables the fabrication of COF-protected Zn anode with an ultra-large area ($>200\ cm^2$) (Figure 1j).

Morphology observation was conducted to study the longitudinal Zn growth mode before and after COF protection of Zn anode. As shown in Figure 2(a), the morphology of bare Zn anode surface changes a bit under a low areal capacity of $1\ mAh\ cm^{-2}$, only small deposited Zn clusters and sparsely distributed basic zinc sulfate can be observed. However, when increasing the capacity to $2\ mAh\ cm^{-2}$, remarkable Zn dendrite appears, which rapidly grows with a larger size of about $20\ \mu m$ after further growth for $5\ mAh\ cm^{-2}$. The cross-section SEM image uncovers that these Zn dendrites are vertically grown on Zn anode toward electrolyte and demonstrate apparent aeolotropy along the surface of Zn anode (Figure 2b). In comparison, after introducing COF on Zn anode, Zn anode could consistently maintain a smooth surface during the gradual capacity increase from 1 to $5\ mAh\ cm^{-2}$ (Figure 2c). At high areal capacity, for example $5\ mAh\ cm^{-2}$, some Zn deposition can be seen on the surface of COF layer. However, no large sized Zn plates can be found, and the surface keeps uniform. This can also be confirmed by the cross-section SEM image in Figure 2(d). To directly study longitudinal Zn growth mode, we then employed in situ optical microscope to observe the Zn deposition process from the perspective of cross section. As shown in Figure 2(e), the bare Zn anode sustains a smooth surface in the initial 10 min, whereas tiny protuberance appears after deposition for 20 min. This protuberance was observed to grow into apparent Zn dendrites in the following 10 min Zn growth, forming a rough surface along Zn anode. In comparison, Zn@COF anode maintains a smooth surface during the whole deposition/growth process (Figure 2f), even at a large areal deposition capacity of $10\ mAh\ cm^{-2}$ (Figure S4). Meanwhile, the expansion of COF layer was observed during Zn deposition, with a 43% expansion rate (Figure S5). The COF layer morphology (Figure S3a) and the porous Zn deposition growth beneath the COF layer (Figure S3b) were further

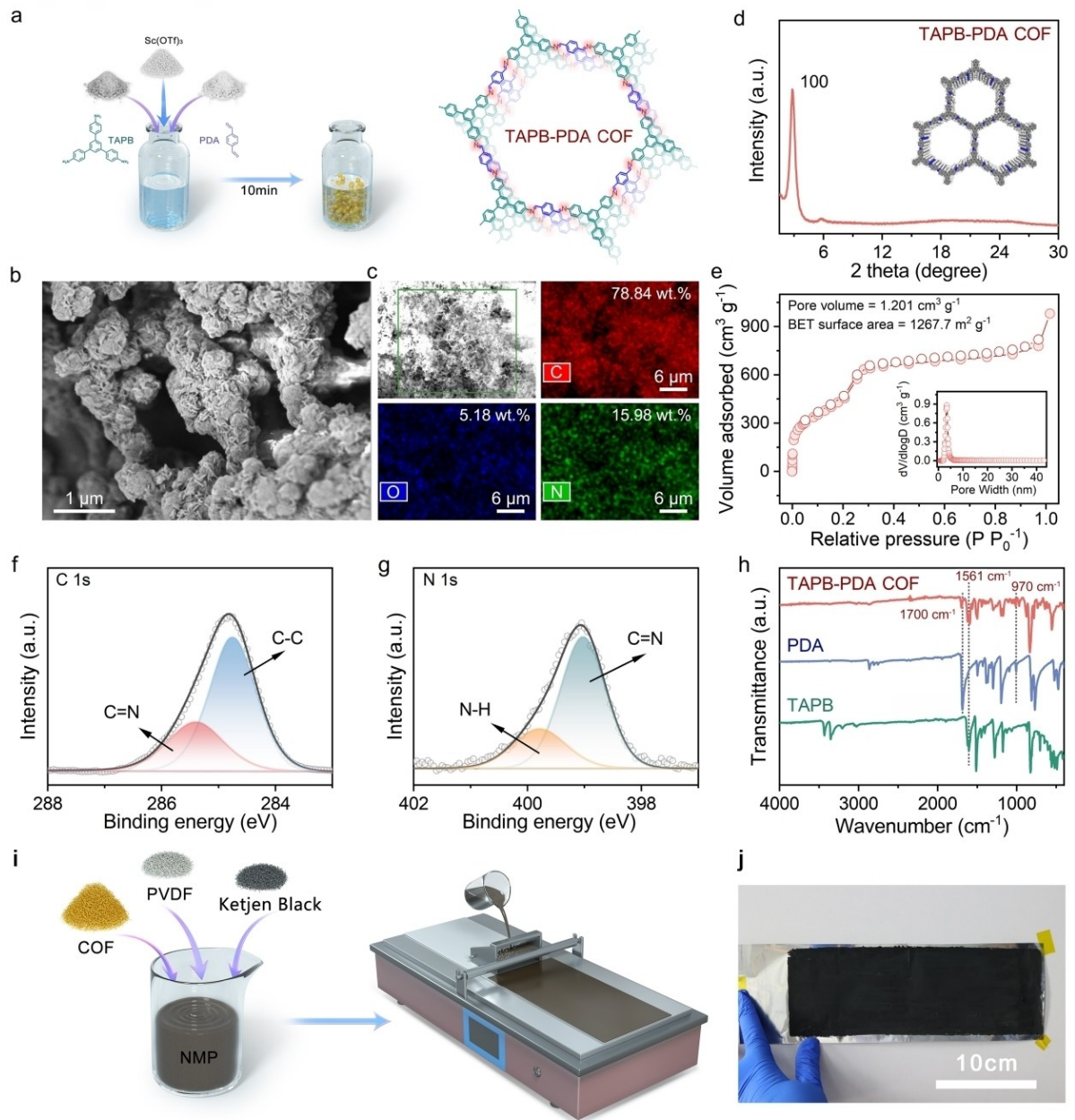


Figure 1. Characterization of COF and its integration with Zn anode. a) Diagram of synthesis method and molecular structure of TAPB-PDA COF. b) SEM image and c) EDS mapping of TAPB-PDA COF. d) PXRD pattern of TAPB-PDA COF. e) N_2 adsorption and desorption curves of TAPB-PDA COF powder. The inset shows the pore size distribution. f) C1s and g) N1s XPS spectra of TAPB-PDA COF. h) FTIR spectra of TAPB-PDA, TAPB, and BDA. i) Diagram of scaleup preparation of COF-protected Zn anode. j) Photo of ultra-large area ($> 200 \text{ cm}^2$) COF-protected Zn anode.

investigated using SEM, which clearly shows the longitudinal Zn growth. All these results suggest the uniform longitudinal Zn growth in the internal space of the COF layer induced by the interaction between Zn and COF. According to the above-mentioned results, it can be concluded that Zn deposition mode can be divided into two types: 1) Zn deposition at the interface domain under low areal capacity and 2) Zn growth in the external space beyond the interface under high areal capacity. The interface Zn deposition with low areal capacity mainly proceeds in a relatively uniform way. The external space Zn growth with high areal capacity tends to happen the

random dendrite growth, which should be addressed by spatial guiding such as COF layer in this work (Figure 2g and h).

To get an insight into the regulation mechanism of longitudinal Zn growth by COF, we employed theoretical computation to study the interaction between Zn and COF. Figure 3(a) exhibits the stable molecule structure of TAPB-PDA COF after optimization. The molecular electrostatic potential diagram reveals that N atoms that linked the TAPB and PDA monomers are negative charge centers^[38] (Figure 3b). TAPB-PDA COF was examined to generally show negative charge property as quantified by zeta potential of -28 mV in aqueous

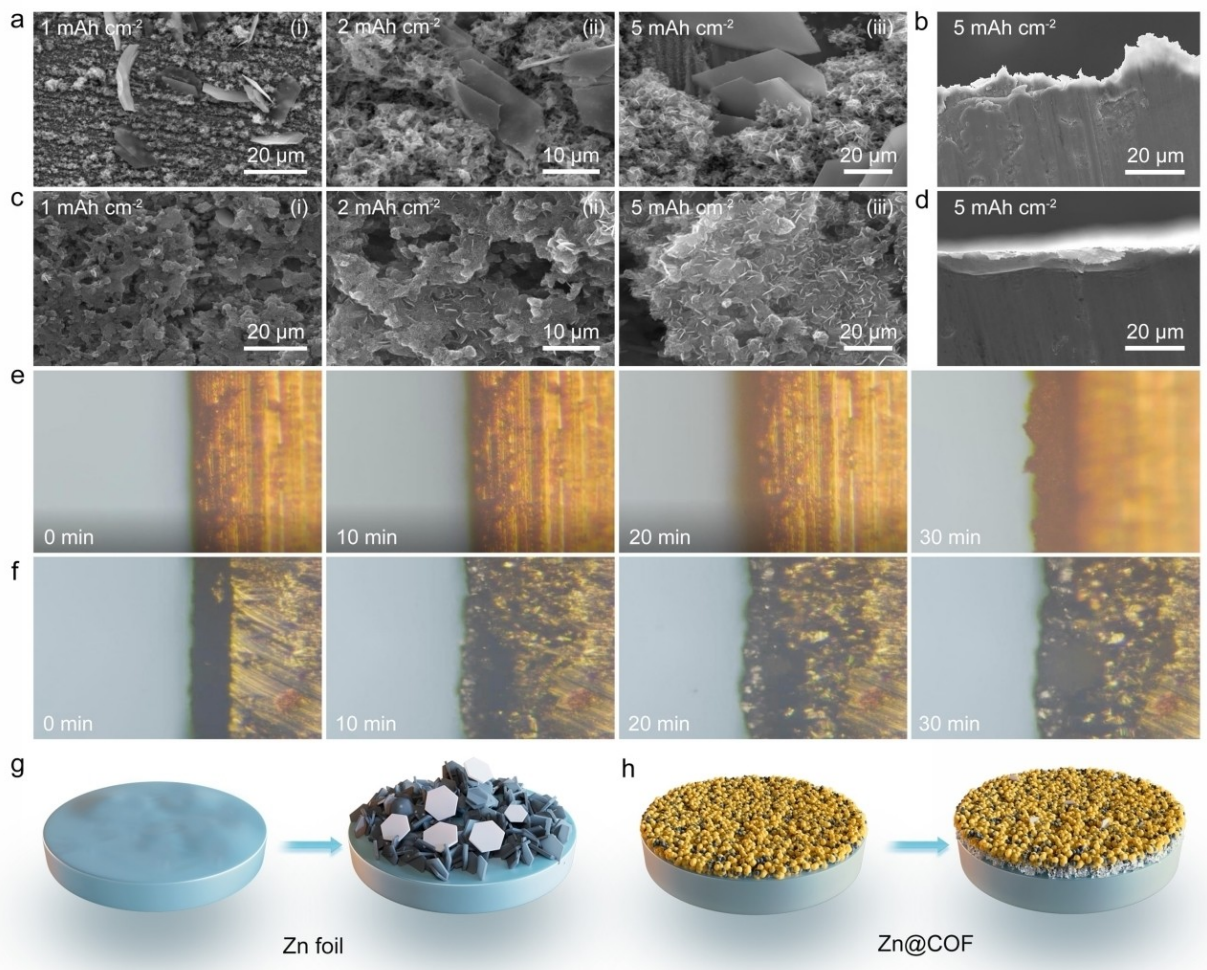


Figure 2. Investigation of longitudinal Zn growth mode. Ex situ SEM images of a) bare Zn and c) Zn@COF at different deposition capacity of 1, 2, and 5 mAh cm^{-2} . Cross-section SEM images of b) bare Zn and d) Zn@COF after depositing for 5 mAh cm^{-2} . In situ optical microscope images of e) bare Zn and f) Zn@COF during the real-time observation of 30 min. g and h) Schematic illustration shows the longitudinal Zn growth mode without or with COF protection.

medium.^[39,40] In addition, the adsorption energy between Zn and COF at two different sites of N and benzene ring was calculated to be -0.964 and -0.156 eV, respectively (Figure 3c), suggesting that there is apparent chemisorption. The calculated differential charge density clearly revealed electron transfer at Zn and N sites (C=N-C node), as shown in Figure 3(d). The yellow and cyan isosurfaces represent the region in which electron density increases ($\Delta\rho = +0.005 \text{ eV}/\text{\AA}^3$) and decreases ($\Delta\rho = -0.005 \text{ eV}/\text{\AA}^3$) after Zn-ion adsorption, respectively. $\Delta\rho$ is the difference of electron density before and after adsorption. Electrostatic interaction and chemisorption serve as the driving force to guide the uniform longitudinal Zn growth in external space beyond interface. Hydrophilic tests demonstrate that COF is much more hydrophobic than Zn metal as quantified by the contact angle of 141.33° for COF and 57.96° for Zn (Figure 3e, f). The hydrophobic interlayer may facilitate the desolvation of hydrated Zn^{2+} in electrolyte.^[41–43] The Tafel plots indicate Zn@COF delivers a much lower exchange current density 0.98 mA cm^{-2} than that 1.14 mA cm^{-2} of bare Zn (Figure 3g). Electrochemical impedance spectroscopy (EIS) measurements show that the impedance gradually decreased

with proceeding the Zn plating/stripping due to the uniform Zn growth which produces intimate contact among battery components (Figure 3h, Table S1).^[44,45] Therefore, the uniform longitudinal Zn growth is attributed to the electrostatic and chemical interaction brought by anodic and N-rich COF. In addition, the hydrophobicity of COF also suppresses the parasitic reaction (Figure 3i).

Symmetric cells were assembled to test the influence of COF on Zn deposition stability. The rate performance examination carried out at varied current densities of 0.2 – 5 mA cm^{-2} shows that Zn@COF || Zn@COF symmetric cell exhibits lower voltage hysteresis than that of the Zn || Zn symmetric cell in the whole current density range (Figure 4e). A much smaller Zn nucleation overpotential was also detected (Figure S6), suggesting that COF modification facilitates the nucleation process of Zn. Meanwhile, Zn@COF || Zn@COF shows gradually increased voltage hysteresis with enlarged current density, which is because of the concentration polarization caused by the rapid Zn^{2+} consumption at large current density (Figure 4a). Meanwhile, we also conducted the comparison of rate capability employing conductive carbon as the coating layer, which

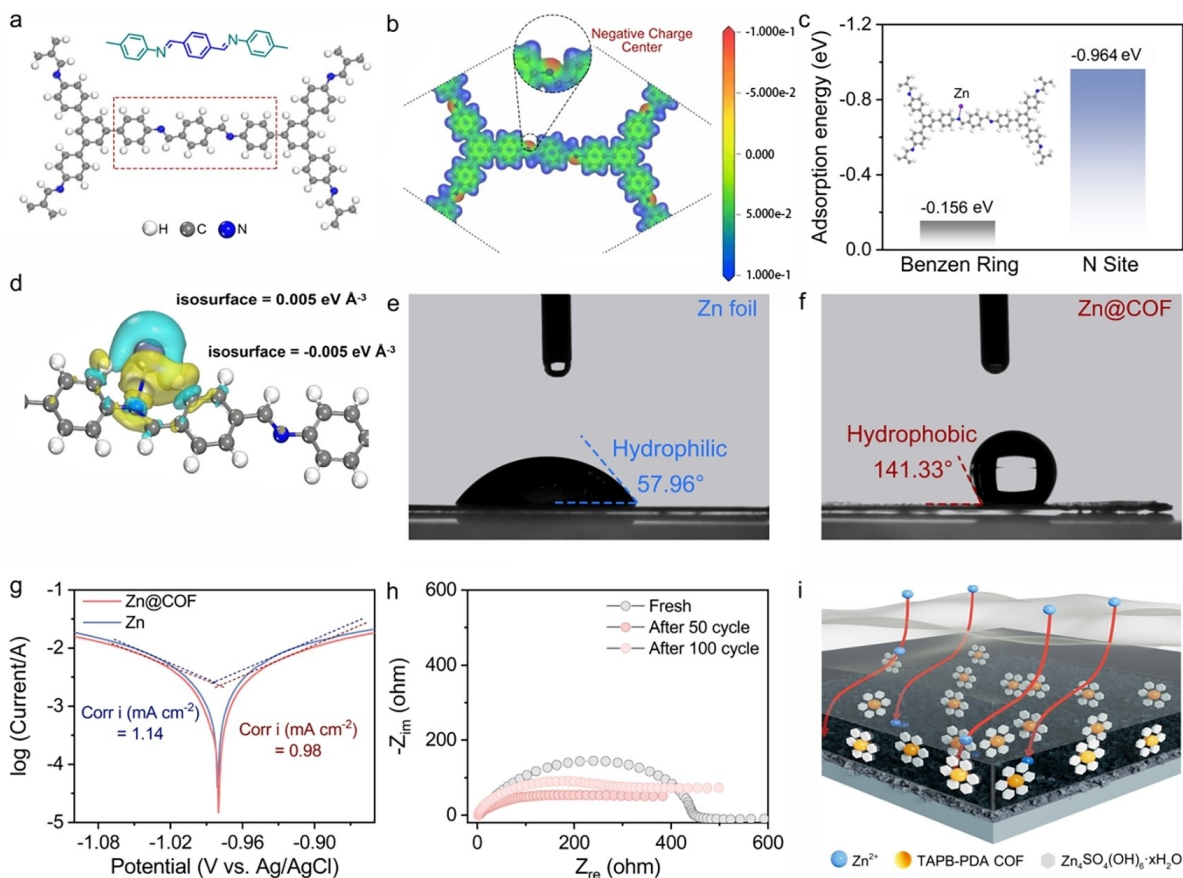


Figure 3. Theoretical and experimental analysis of longitudinal Zn growth induced by COF. a) Molecule structure and b) Molecular electrostatic potential diagram of TAPB-PDA COF. c) The adsorption between Zn and TAPB-PDA COF. d) Isosurface charge density plot of COF–Zn. Contact angle test of e) Zn and f) Zn@COF using water. g) Tafel plots recorded at the scanning rate 1 mVs^{-1} with marking the exchange current densities. h) EIS data of Zn@COF symmetric cell before and after cycling. i) Schematic diagram shows the uniform longitudinal Zn growth induced by COF and evenly distributed basic zinc sulfate guided by COF.

suffers from a rapid increase of voltage hysteresis after only 150 h, further demonstrating the key role of COF interface in safeguarding Zn anode and highlighting the selectivity of interface layer (Figure S7). For cycling stability, the $\text{Zn}||\text{Zn}$ symmetric cell tested at 5 mA cm^{-2} shows short circuit after only 154 h, whereas $\text{Zn@COF}||\text{Zn@COF}$ symmetric cell runs stably after 1000 h, remarkably prolonging the lifespan by an ultrahigh proportion of up to 550% (Figure 4b). In addition, the enlarged voltage-time curves in Figure 4c exhibit that after introducing COF interface on Zn anode, the voltage hysteresis of Zn plating/stripping could be apparently decreased from about 212 to 124 mV. This is proposed by previous work to be related to the accelerated desolvation kinetics of hydrated zinc ions.^[46,47] During the long-term cycling examination, $\text{Zn@COF}||\text{Zn@COF}$ symmetric cell only shows a tiny increase of voltage hysteresis of 12 mV (Figure 4d, e), corresponding to a low proportion of less than 10%, reflecting the great potential of using this anodic COF to stabilizing Zn metal anode. The thickness of the COF layer affects the voltage hysteresis and the cycling property. Due to the strong insulation of COF, a thick COF layer coated sample results in a large polarization and an early failure during cycling (Figure S8). The thin COF layer leads to weakened guidance effects to the Zn^{2+} . A

moderate mass loading of $0.3\text{--}0.8 \text{ mg cm}^{-2}$ was found to be appropriate. After cycling 1000 h, the COF layer is mechanically stable, even though there are deformations due to the compression of cell assembly, no cracks were observed (Figure S9), the TAPB-PDA COF related peaks are partially preserved in the FTIR spectrum (Figure S10).

We further examined the improvement of $\text{Zn}-\text{I}_2$ full batteries by introducing COF. The cyclic voltammetry (CV) curves tested at 2 mVs^{-1} show that $\text{Zn@COF}||\text{AC}+\text{I}_2$ battery delivers a higher potential of anodic peak than $\text{Zn}||\text{AC}+\text{I}_2$ battery by 60 mV (Figure 5a). Series of CV curves recorded at 1, 2, 3, 5, 8, and 10 mVs^{-1} demonstrates that with increasing the scanning rate, the anodic peak that corresponds to the reduction of I_2 to I^- shows a slight shift, indicating the highly efficient ion diffusion achieved by the introduction of COF (Figure 5b). Galvanostatic charge and discharge (GCD) curves tested at 0.3 Ag^{-1} reveal that $\text{Zn@COF}||\text{AC}+\text{I}_2$ battery delivers a higher specific capacity than the bare Zn case (Figure 5c). We then examined the rate performance of the $\text{Zn}-\text{I}_2$ batteries before and after introducing COF layer at varied current densities of $0.3\text{--}5 \text{ Ag}^{-1}$ (Figure 5d). $\text{Zn@COF}||\text{AC}+\text{I}_2$ battery releases higher specific capacities than the bare Zn case during the whole range of current densities, which is in good accordance with

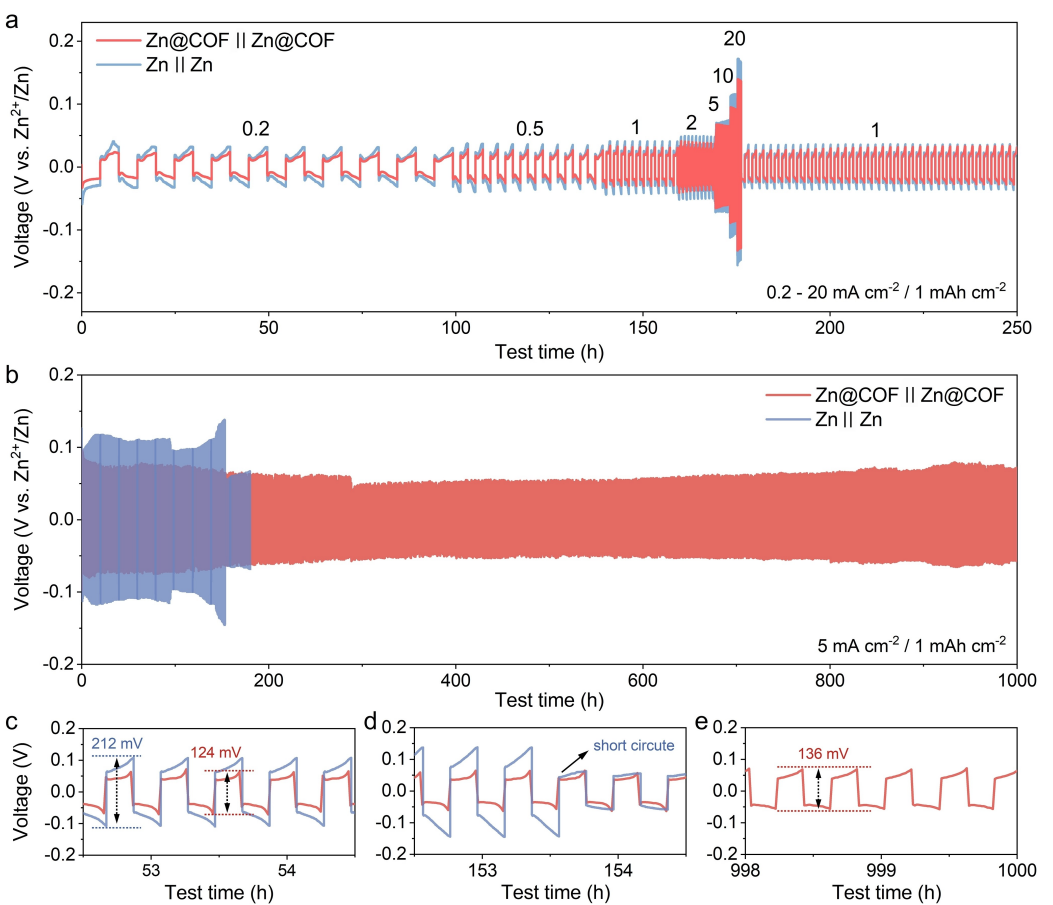


Figure 4. Electrochemical performance of Zn symmetric cells with or without COF. a) Rate capability of symmetric cells at varied current densities of 0.2–20 mA cm⁻² with an areal capacity of 1 mAh cm⁻². b) Cycling performance of symmetric cells tested at 5 mA cm⁻² and 1 mAh cm⁻². c–e) The enlarged voltage–time curves tested at different time.

the CV curves. It is found that with increasing the current densities from 0.3 to 5 A g⁻¹, the discharge potential maintains relatively stable as shown in the corresponding GCD curves, further indicating the suppression of battery polarization by COF (Figures 5e, S11). Long term cycling performance examined at the I₂ loading mass of 1.95 mg cm⁻² and 1 A g⁻¹ demonstrates Zn@COF||AC+I₂ battery's superior cycling stability of sustaining a high capacity retention and high coulombic efficiency (near 100%) after 10000 cycles, which is much better than the bare Zn case (Figure S12). When increasing the I₂ loading mass to 7.8 mg cm⁻², Zn||AC+I₂ battery encounters sharp capacity decay after only 300 cycles, while Zn@COF||AC+I₂ battery could maintain a very high capacity retention of near 100% after 1000 cycles (Figure 5f). These above-mentioned results demonstrate that COF can guide the uniform longitudinal Zn growth and thus improve the cycling and rate performance of Zn-I₂ battery. Compared with recently reported Zn-I₂ batteries, Zn@COF||AC+I₂ batteries exhibits superior performance (Table S2).

Conclusions

This work highlights the key role of longitudinal Zn growth in external space beyond the interface domain in practical Zn metal anode with requirement of high areal capacity and reports an anodic COF to guide uniform Zn growth. In situ optical microscope observation directly confirm the formation of smooth surface even after Zn plating for a high areal capacity of 10 mA cm⁻². Theoretical calculation and zeta potential test reveal the negative charge property of COF and the chemisorption to Zn at its N atom sites, statically and chemically attracting zinc to realize the uniform longitudinal Zn growth. In addition, COF layer was examined by contact angle test to be hydrophobic, which could physically isolate Zn anode from aqueous electrolyte and thus effectively suppress water decomposition and avoid the formation of alkaline zincate on Zn metal surface. Benefiting from this stable longitudinal Zn growth, the Zn@COF symmetric cell achieves enhancement of cycling lifespans associated with lower voltage hysteresis than the bare Zn case. Moreover, Zn@COF||AC+I₂ full battery achieves a long cycling life of 10000 cycles with a high coulombic efficiency of near 100%. It should be noted that the introduction of COF layer on Zn anode could also promote the rate performance. Our work sheds light on the development of

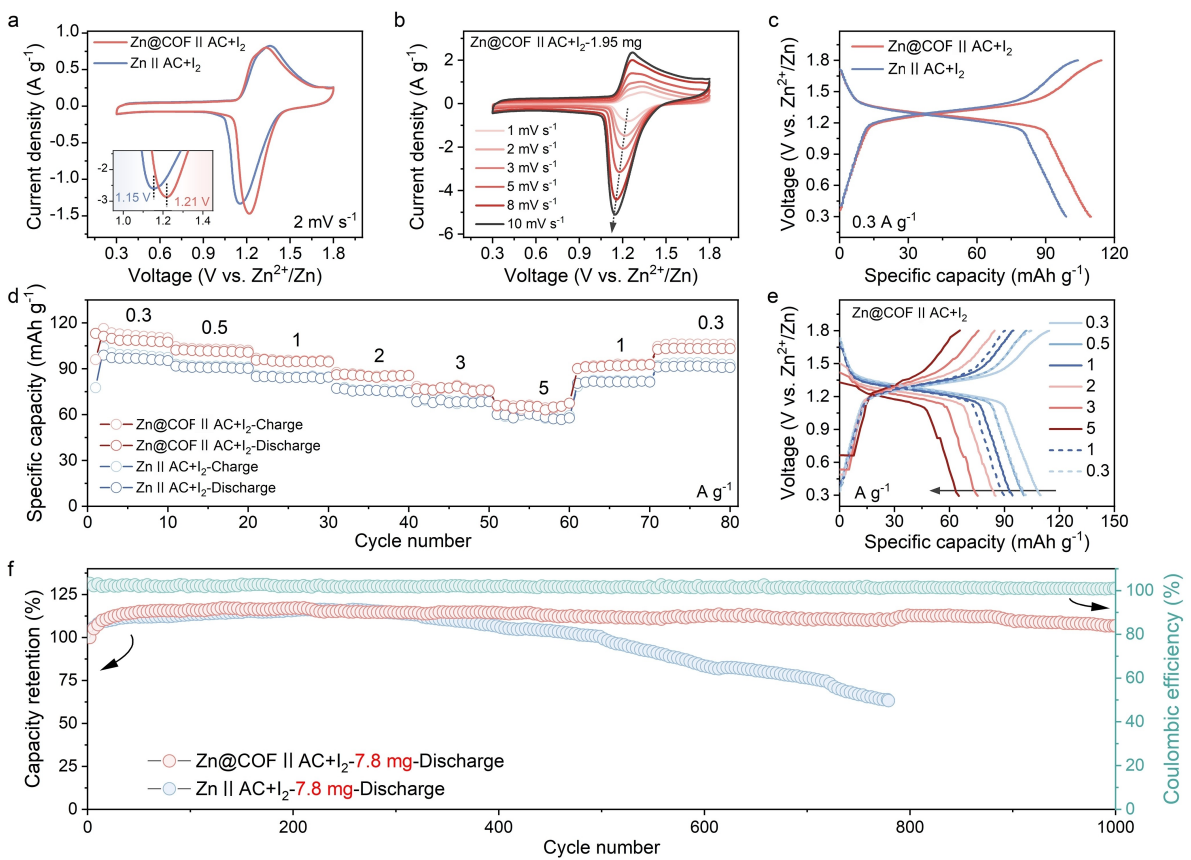


Figure 5. Electrochemical performance of Zn-I₂ full batteries. a) CV curves of Zn-I₂ batteries with bare Zn and Zn@COF as anodes recorded at 2 mVs⁻¹. b) CV curves recorded at different scan rates of 1–10 mVs⁻¹. c) GCD curves of Zn-I₂ batteries using different anodes at 0.3 A g⁻¹. d) Rate performance tested at various current densities of 0.3–5 A g⁻¹ and e) the corresponding GCD curves. f) Long term cycling performance tested at I₂ loading mass of 7.8 mg cm⁻².

practical Zn metal anode with high areal capacity from the perspective of longitudinal Zn growth in the external space beyond interface.

Experimental Section

TAPB-PDA COF synthesis. TAPB-PDA COF was prepared according to previous work.^[48] Specifically, 1,3,5-tris(4-aminophenyl)benzene (36 mg, 0.10 mmol) and terephthalaldehyde (20 mg, 0.15 mmol) were dissolved in 1,4-dioxane/mesitylene solution (4:1 v/v, 4.0 mL) through sonication at room temperature. Then, scandium(III) trifluoromethanesulfonate (3.0 mg, 6.0 µmol) was added, and the resulting suspension was sonicated briefly. The vial was closed with a plastic cap for 10 minutes. With the reaction proceeding, precipitates were activated by Soxhlet extraction using CH₃OH for 12 h, followed by supercritical CO₂ drying, obtaining TAPB-PDA COF.

Material characterizations. The morphology images of COF particles were observed on a Thermo Fischer Apreo field-emission scanning electron microscopy (FE-SEM), along with corresponding elemental dispersive spectroscopy (EDS). The morphology images of Zn electrode and Zn@COF electrode were observed on Hitachi SU8010 FE-SEM. Powder X-ray diffraction (PXRD) data was recorded on a Rigaku MiniFLEX 600 instrument operating at 40 kV voltage and 50 mA current with a monochromatized Cu-K α ($\lambda = 1.54056 \text{ \AA}$). Samples were mounted as integral films onto a silicon zero background holder. The PXRD patterns were tested at the range of

1.5 to 30 degree with a step size of 0.02 degree and scan rate of 10 degree min⁻¹. N₂ adsorption and desorption was conducted at 77 K by using Quantachrome Instrument ASiQMVH002-5 after pretreating samples by heating under vacuum at 120 °C for 12 h. The pore size distributions were calculated using the non-localized density functional theory (NLDFT). All samples were tested using nitrogen with a high purity of 99.999%. X-ray photoelectron spectroscopy (XPS) was performed on a Thermo Fisher ESCALAB Xi + spectrometer equipped with Al K α radiation to characterize the surface components. FTIR-ATR spectra were recorded at the range of 400–4000 cm⁻¹ on a Bruker ALPHA spectrometer. The contact Angle is measured on Shanghai Powereach JC2000D1 contact angle meter.

Electrochemical measurement. To prepare the COF modified Zn electrode (i.e., Zn@COF), TAPB-PDA COF, ketjen black and polyvinylidene difluoride (PVDF) binder were mixed in a mass ratio of 6:3:1 in N-Methylpyrrolidone (NMP) solvent to form a uniformly slurry. Then the slurry was gently scraped and coated on zinc plates with size of 1×1 cm, and dried at 60 °C for 12 h in vacuum. The mass loading of active materials (i.e., TAPB-PDA COF) is 0.3–0.8 mg cm⁻².

Tafel measurements: Three-electrode beaker cells were first assembled with as-prepared Zn or Zn@COF electrode (1×1 cm) as working electrode, Pt as the counter electrode and Ag/AgCl as the reference electrode. The distance between each electrode is around 1 cm. The electrolyte employed was 8 mL aqueous 1 M ZnSO₄ (99.9% metals basis, Aladdin) solution. Then experiment Tafel measurements was carried out on a CHI760E electrochemical

workstation within voltage range of $-0.4\text{--}1.4\text{ V}$ under scan rate of 1 mV s^{-1} .

In-situ optical microscopy measurements: $\text{Zn}||\text{Zn}$ or $\text{Zn}@\text{COF}||\text{Zn}@\text{COF}$ symmetric cells were installed in an in situ two-electrode electrolysis cell and the electrolyte employed was 1 M ZnSO_4 (99.9% metals basis, Aladdin) aqueous solution for observation under an optical industrial microscope (KY-H3800S42, KangYuan Electronic). The cells were cycled at current densities of 10 mA cm^{-2} under the fixed Zn plating capacity of 1 mAh cm^{-2} and 10 mAh cm^{-2} .

Zinc nucleation overpotential of metal deposition: Zinc foil ($100\text{ }\mu\text{m}$) were sliced into round pieces with diameter 12 mm , dipped in ethyl alcohol and cleaned by ultrasound for 15 min , as the counter electrode (CE). And the Zinc foil with COF coating ($\text{Zn}@\text{COF}$) were sliced into same round pieces of diameter 12 mm , as the working electrode (WE). To eliminate the influence of stripping overpotential on zinc counter electrode (CE), a piece of zinc foil ($3\times100\text{ mm}$) were used as the reference electrode (RE). Three electrode were embedded into an electrolytic cell with three openings, infiltrated by 15 mL electrolyte(1 M ZnSO_4). Each deposition of zinc was under 5 mA cm^{-2} steady current densities for 12 min (1 mAh cm^{-2}).

For $\text{Zn}||\text{Zn}$ symmetric cells, two zinc plates (bare Zn or $\text{Zn}@\text{COF}$) were used as electrodes, glass fiber ($\phi=18\text{ mm}$) acted as separator, and 1 M ZnSO_4 aqueous solution was used as the electrolyte. The electrochemical performance of Zn–Zn symmetric cells was evaluated by assembling CR2032-type coin cells. The symmetric cells were cycled at various current densities from 0.2 to 5 mA cm^{-2} under the fixed Zn plating capacity of 1 mAh cm^{-2} , respectively.

In addition, for $\text{Zn}||\text{AC+I}_2$ full cells, the AC+I_2 cathode was prepared as follows: the cathode electrode was fabricated by mixing the active carbon, ketjen black and polyvinylidene difluoride (PVDF) binder (according to the mass ratio of $7:2:1$) in N-Methylpyrrolidone (NMP) solvent and stirred to form a uniformly slurry. The slurry is then scraped and coated on the graphite paper, and then in a vacuum oven at 60°C for 12 h . After drying, the electrode slice ($\phi=14\text{ mm}$) was placed in a 1 M ZnI_2 (99%, Innochem) solution for 4 h . After drying at 60°C for 12 h , the AC+I_2 cathode electrode was obtained.

Zn-AC+I_2 full cells were assembled with bare Zn or a $\text{Zn}@\text{COF}$ as anode, glass fiber ($\phi=18\text{ mm}$) acted as separator, AC+I_2 as cathode, and 1 M ZnSO_4 aqueous solution as electrolyte. Galvanostatic charge/discharge cycling measurements were carried out on a LAND multichannel battery testing system (CT3001 A, China) within voltage range of $0.3\text{--}1.8\text{ V}$ under current densities of 0.3 , 0.5 , 1.0 , 2.0 , 3.0 , and 5.0 A g^{-1} . Cyclic voltammetry (CV) testing was performed on CHI760E electrochemical workstation (Chenhua, China) with scan rate of $1\text{--}10\text{ mV s}^{-1}$ and potential range of $0.3\text{--}1.8\text{ V}$. Electrochemical impedance spectroscopy (EIS) measurements were carried out using a Gamry electrochemical workstation with frequencies ranging from 10^5 to 10^{-2} Hz and the voltage amplitude of 10 mV .

Computational methods. We employed the Vienna Ab Initio Package (VASP)^[49,50] to perform all the density functional theory (DFT) calculations within the generalized gradient approximation (GGA) using the PBE^[51] formulation. We have chosen the projected augmented wave (PAW)^[52,53] potentials to describe the ionic cores and take valence electrons into account using a plane wave basis set with a kinetic energy cutoff of 400 eV . Partial occupancies of the Kohn-Sham orbitals were allowed using the Gaussian smearing method and a width of 0.05 eV . The electronic energy was considered self-consistent when the energy change was smaller than 10^{-4} eV . A geometry optimization was considered convergent

when the force change was smaller than $0.03\text{ eV}/\text{\AA}$. Grimme's DFT-D3 methodology^[54] was used to describe the dispersion interactions. The equilibrium lattice constants of COF unit cell were optimized, when using a $2\times2\times2$ Monkhorst-Pack k-point grid for Brillouin zone sampling. Finally, the adsorption energies (E_{ads}) are calculated as $E_{\text{ads}} = E_{\text{ad/sub}} - E_{\text{ad}} - E_{\text{sub}}$, where $E_{\text{ad/sub}}$, E_{ad} and E_{sub} are the optimized adsorbate/substrate system, the adsorbate in the structure and the clean substrate respectively.

Acknowledgements

The authors acknowledge the financial support by the National Natural Science Foundation of China (Grant No. 21625102, and 21471018); the China National Petroleum Corporation Research Fund Program; and the Research Institute of Petroleum Exploration and Development Research Fund Program.

Conflict of Interests

The authors declare no conflict of interest.

Data Availability Statement

The data that support the findings of this study are available in the supplementary material of this article. Original data are available from the authors on a reasonable request.

Keywords: covalent organic framework · high areal capacity · interfacial spatial · longitudinal zinc growth · zinc dendrite

- [1] L. Cao, D. Li, T. Pollard, T. Deng, B. Zhang, C. Yang, L. Chen, J. Vatamanu, E. Hu, M. J. Hourwitz, L. Ma, M. Ding, Q. Li, S. Hou, K. Gaskell, J. T. Fourkas, X. Yang, K. Xu, O. Borodin, C. Wang, *Nat. Nanotechnol.* **2021**, *16*, 902–910.
- [2] A. Kundu, S. Mallick, S. Ghora, C. R. Raj, *Acs Appl. Mater. Interfaces* **2021**, *13*, 40172–40199.
- [3] Y. Liang, H. Dong, D. Aurbach, Y. Yao, *Nat. Energy* **2020**, *5*, 646–656.
- [4] W. Sun, F. Wang, B. Zhang, M. Zhang, V. Küpers, X. Ji, C. Theile, P. Bieker, K. Xu, C. Wang, M. Winter, *Science* **2021**, *371*, 46–51.
- [5] B. Tang, L. Shan, S. Liang, J. Zhou, *Energy Environ. Sci.* **2019**, *12*, 3288–3304.
- [6] L. Qian, W. Yao, R. Yao, Y. Sui, H. Zhu, F. Wang, J. Zhao, C. Zhi, C. Yang, *Adv. Funct. Mater.* **2021**, *31*, 2105736.
- [7] S. Mallick, C. R. Raj, *Chemsuschem* **2021**, *14*, 1987–2022.
- [8] M. Song, H. Tan, D. Chao, H. J. Fan, *Adv. Funct. Mater.* **2018**, *28*, 1802564.
- [9] J. Hao, X. Li, S. Zhang, F. Yang, X. Zeng, S. Zhang, G. Bo, C. Wang, Z. Guo, *Adv. Funct. Mater.* **2020**, *30*, 2001263.
- [10] W. Du, E. H. Ang, Y. Yang, Y. Zhang, M. Ye, C. C. Li, *Energy Environ. Sci.* **2020**, *13*, 3330–3360.
- [11] F. Xie, H. Li, X. Wang, X. Zhi, D. Chao, K. Davey, S. Z. Qiao, *Adv. Energy Mater.* **2021**, *11*, 2003419.
- [12] C. Xu, B. Li, H. Du, F. Kang, *Angew. Chem. Int. Ed.* **2012**, *51*, 933–935.
- [13] W. Sun, F. Wang, S. Hou, C. Yang, X. Fan, Z. Ma, T. Gao, F. Han, R. Hu, M. Zhu, C. Wang, *J. Am. Chem. Soc.* **2017**, *139*, 9775–9778.
- [14] M. Han, J. Huang, S. Liang, L. Shan, X. Xie, Z. Yi, Y. Wang, S. Guo, J. Zhou, *Iscience* **2020**, *23*, 100797.
- [15] Q. Yang, F. Mo, Z. Liu, L. Ma, X. Li, D. Fang, S. Chen, S. Zhang, C. Zhi, *Adv. Mater.* **2019**, *31*, 1901521.
- [16] J. Ding, Z. Du, L. Gu, B. Li, L. Wang, S. Wang, Y. Gong, S. Yang, *Adv. Mater.* **2018**, *30*, 1800762.

- [17] P. Liang, J. Yi, X. Liu, K. Wu, Z. Wang, J. Cui, Y. Liu, Y. Wang, Y. Xia, J. Zhang, *Adv. Funct. Mater.* **2020**, *30*, 1908528.
- [18] Z. Guo, Y. Ma, X. Dong, J. Huang, Y. Wang, Y. Xia, *Angew. Chem. Int. Ed.* **2018**, *57*, 11737–11741.
- [19] F. Wan, L. Zhang, X. Wang, S. Bi, Z. Niu, J. Chen, *Adv. Funct. Mater.* **2018**, *28*, 1804975.
- [20] Q. Yang, Q. Li, Z. Liu, D. Wang, Y. Guo, X. Li, Y. Tang, H. Li, B. Dong, C. Zhi, *Adv. Mater.* **2020**, *32*, 2001854.
- [21] Y. Li, Y. Wang, Y. Shi, H. Wu, J. Zeng, H. Bu, M. Zhu, C. Xiao, Y. Zhang, G. Gao, S. Ding, *Sci. Bull.* **2020**, *65*, 1094–1102.
- [22] X. Zeng, J. Mao, J. Hao, J. Liu, S. Liu, Z. Wang, Y. Wang, S. Zhang, T. Zheng, J. Liu, P. Rao, Z. Guo, *Adv. Mater.* **2021**, *33*, 2007416.
- [23] Q. Yang, G. Liang, Y. Guo, Z. Liu, B. Yan, D. Wang, Z. Huang, X. Li, J. Fan, C. Zhi, *Adv. Mater.* **2019**, *31*, 1903778.
- [24] Q. Yang, L. Li, T. Hussain, D. Wang, L. Hui, Y. Guo, G. Liang, X. Li, Z. Chen, Z. Huang, Y. Li, Y. Xue, Z. Zuo, J. Qiu, Y. Li, C. Zhi, *Angew. Chem. Int. Ed.* **2022**, *61*, 202112304.
- [25] J. Hao, B. Li, X. Li, X. Zeng, S. Zhang, F. Yang, S. Liu, D. Li, C. Wu, Z. Guo, *Adv. Mater.* **2020**, *32*, 2003021.
- [26] B. Wu, W. Luo, M. Li, L. Zeng, L. Mai, *Nano Res.* **2021**, *14*, 3174–3187.
- [27] Q. Zhang, J. Luan, L. Fu, S. Wu, Y. Tang, X. Ji, H. Wang, *Angew. Chem. Int. Ed.* **2019**, *58*, 15841–15847.
- [28] F. Wang, O. Borodin, T. Gao, X. Fan, W. Sun, F. Han, A. Faraone, J. A. Dura, K. Xu, C. Wang, *Nat. Mater.* **2018**, *17*, 543–549.
- [29] H. Qiu, X. Du, J. Zhao, Y. Wang, J. Ju, Z. Chen, Z. Hu, D. Yan, X. Zhou, G. Cui, *Nat. Commun.* **2019**, *10*, 5374.
- [30] Y. Wu, Y. Tao, X. Zhang, K. Zhang, S. Chen, Y. Liu, Y. Ding, M. Cai, X. Liu, S. Dai, *Sci. China Mater.* **2020**, *63*, 1196–1204.
- [31] C. Li, Z. Sun, T. Yang, L. Yu, N. Wei, Z. Tian, J. Cai, J. Lv, Y. Shao, M. H. Rümmeli, J. Sun, Z. Liu, *Adv. Mater.* **2020**, *32*, 2003425.
- [32] M. Zhu, J. Hu, Q. Lu, H. Dong, D. D. Karnaushenko, C. Becker, D. Karnaushenko, Y. Li, H. Tang, Z. Qu, J. Ge, O. G. Schmidt, *Adv. Mater.* **2021**, *33*, 2007497.
- [33] T. Xue, H. J. Fan, *J. Energy Chem.* **2021**, *54*, 194–201.
- [34] Z. Zhao, R. Wang, C. Peng, W. Chen, T. Wu, B. Hu, W. Weng, Y. Yao, J. Zeng, Z. Chen, P. Liu, Y. Liu, G. Li, J. Guo, H. Lu, Z. Guo, *Nat. Commun.* **2021**, *12*.
- [35] J. Zhao, Y. Ying, G. Wang, K. Hu, Y. D. Yuan, H. Ye, Z. Liu, J. Y. Lee, D. Zhao, *Energy Storage Mater.* **2022**, *48*, 82–89.
- [36] C. Guo, J. Zhou, Y. Chen, H. Zhuang, Q. Li, J. Li, X. Tian, Y. Zhang, X. Yao, Y. Chen, S. L. Li, Y. Q. Lan, *Angew. Chem. Int. Ed.* **2022**, *134*, e202210871.
- [37] B. J. Smith, A. C. Overholts, N. Hwang, W. R. Dichtel, *Chem. Commun.* **2016**, *52*, 3690–3693.
- [38] R. Gomes, P. Bhanja, A. Bhaumik, *Chem. Commun.* **2015**, *51*, 10050–10053.
- [39] C. Sun, C. Wu, X. Gu, C. Wang, Q. Wang, *Nano-Micro Lett.* **2021**, *13*, 89.
- [40] J. Zhang, W. Peng, J. Jin, S. Yang, A. Yu, G. Li, *Sci. China Mater.* **2022**, *65*, 663–674.
- [41] S. H. Park, S. Y. Byeon, J. Park, C. Kim, *Acs Energy Lett.* **2021**, *6*, 3078–3085.
- [42] Z. Cao, P. Zhuang, X. Zhang, M. Ye, J. Shen, P. M. Ajayan, *Adv. Energy Mater.* **2020**, *10*, 2001599.
- [43] D. Han, S. Wu, S. Zhang, Y. Deng, C. Cui, L. Zhang, Y. Long, H. Li, Y. Tao, Z. Weng, Q. H. Yang, F. Kang, *Small* **2020**, *16*, 2001736.
- [44] Y. Cui, Q. Zhao, X. Wu, Z. Wang, R. Qin, Y. Wang, M. Liu, Y. Song, G. Qian, Z. Song, L. Yang, F. Pan, *Energy Storage Mater.* **2020**, *27*, 1–8.
- [45] Y. Liang, Y. Wang, H. Mi, L. Sun, D. Ma, H. Li, C. He, P. Zhang, *Chem. Eng. J.* **2021**, *425*, 131862.
- [46] Z. Hou, H. Tan, Y. Gao, M. Li, Z. Lu, B. Zhang, *J. Mater. Chem. A* **2020**, *8*, 19367–19374.
- [47] D. Kundu, S. Hosseini Vajargah, L. Wan, B. Adams, D. Prendergast, L. F. Nazar, *Energy Environ. Sci.* **2018**, *11*, 881–892.
- [48] M. Matsumoto, R. R. Dasari, W. Ji, C. H. Feriante, T. C. Parker, S. R. Marder, W. R. Dichtel, *J. Am. Chem. Soc.* **2017**, *139*, 4999–5002.
- [49] J. Furthmüller, G. Kresse, *Phys. Rev. B* **1996**, *54*, 11169–11186.
- [50] K. Burke, M. Ernzerhof, J. P. Perdew, *Phys. Rev. Lett.* **1996**, *77*, 3865–3868.
- [51] D. Joubert, G. Kresse, *Phys. Rev. B* **1999**, *59*, 1758–1775.
- [52] P. E. Blöchl, *Phys. Rev. B* **1994**, *50*, 17953–17979.
- [53] S. Grimme, J. Antony, S. Ehrlich, H. Krieg, *J. Chem. Phys.* **2010**, *132*, 154104.
- [54] G. Henkelman, B. P. Uberuaga, H. Jónsson, *J. Chem. Phys.* **2000**, *113*, 9901–9904.

Manuscript received: March 10, 2023

Revised manuscript received: March 14, 2023

Accepted manuscript online: April 9, 2023

Version of record online: May 5, 2023